Supplemental Information for: Spin Hamiltonian in the Modulated Momenta of Light

Juan Feng[1], Zengya Li[1], Luqi Yuan[1], Erez Hasman[2], Bo Wang[1,*], Xianfeng Chen[1,3,4]

[1] *State Key Laboratory of Photonics and Communications, School of Physics and Astronomy, Shanghai Jiao Tong University; Shanghai, 200240, China.*

[2] *Atomic-Scale Photonics Laboratory, Russell Berrie Nanotechnology Institute, and Helen Diller Quantum Center, Technion–Israel Institute of Technology; Haifa, 3200003, Israel.*

[3] *Shanghai Research Center for Quantum Sciences; Shanghai, 201315, China.*

[4] *Collaborative Innovation Center of Light Manipulations and Applications, Shandong Normal University; Jinan, 250358, China.*

[*] *wangbo89@sjtu.edu.cn*

Supplementary Note 1. Theoretical Derivation

The spin Hamiltonian of the classical 2D XY model is defined as

$$H_r = -\sum_{j,h} J(\boldsymbol{R}_j - \boldsymbol{R}_h)\boldsymbol{s}_j \cdot \boldsymbol{s}_h = -\sum_{j,h} J(\boldsymbol{r}_{jh})\boldsymbol{s}_j \cdot \boldsymbol{s}_h, \tag{S1}$$

where $\boldsymbol{s}_j$ is a spin at the position of $\boldsymbol{R}_j$. The displacement between two spins is denoted as $\boldsymbol{r}_{jh} = \boldsymbol{R}_j - \boldsymbol{R}_h$, and $J(\boldsymbol{r}_{jh})$ is the interaction strength function. In the XY model, $\boldsymbol{s}_j$ can be represented by a planar rotator θ_j. Therefore, the Hamiltonian is rewritten as

$$H_r = -\sum_{j,h} J(\boldsymbol{r}_{jh}) \cos(\theta_j - \theta_h). \tag{S2}$$

Here, $J(\boldsymbol{r}_{jh})$ can be represented by its Fourier spectrum

$$J(\boldsymbol{r}_{jh}) = \iint_{-\infty}^{\infty} V(\boldsymbol{k}) \mathrm{e}^{-\mathrm{i}(\boldsymbol{r}_{jh}\cdot\boldsymbol{k})} dk_x dk_y, \tag{S3}$$

that is

$$H_r = -\sum_{j,h} \iint_{-\infty}^{\infty} V(\boldsymbol{k}) \mathrm{e}^{-\mathrm{i}(\boldsymbol{r}_{jh}\cdot\boldsymbol{k})} dk_x dk_y \cos(\theta_j - \theta_h), \tag{S4}$$

where $\boldsymbol{r}_{jh} = (x_j - x_h, y_j - y_h)$, $\boldsymbol{k} = (k_x, k_y)$.

In optics, the light field modulated by a spatial light modulator (SLM) is

$$E(x,y) = \sum_j \xi_j \mathrm{e}^{\mathrm{i}\theta_j} \mathrm{rect}_{\Lambda}(x-x_j, y-y_j) = \mathrm{rect}_{\Lambda}(x,y) \otimes \Big(\sum \xi_j \mathrm{e}^{\mathrm{i}\theta_j} \delta(x-x_j, y-y_j) \Big), \quad \text{(S5)}$$

where ξ_j and θ_j are the amplitude and phase of the light field at the position (x_j, y_j). The function $\mathrm{rect}_{\Lambda}(x,y)$ arises from the rectangular shape of the pixel, and Λ is the side length of the pixel. The modulated light field in the momentum space is

$$\tilde{E}(k_x, k_y) = \mathcal{F}\big(\mathrm{rect}_{\Lambda}(x,y)\big) \left(\sum \xi_j \mathrm{e}^{\mathrm{i}\theta_j} \mathcal{F}\big(\delta(x,y)\big) \mathrm{e}^{-\mathrm{i}(k_x x_j + k_y y_j)} \right). \quad \text{(S6)}$$

Note that $\mathrm{rect}_{\Lambda}(x,y) = \mathrm{rect}_{\Lambda}(x)\mathrm{rect}_{\Lambda}(y)$. Hence,

$$\mathcal{F}\big(\mathrm{rect}_{\Lambda}(x,y)\big) = \Lambda \mathrm{sinc}\left(\frac{\Lambda k_x}{2}\right) \Lambda \mathrm{sinc}\left(\frac{\Lambda k_y}{2}\right). \quad \text{(S7)}$$

In this work, we do not consider the amplitude modulations, so we set $\xi_j = 1$. Moreover, we assume that the pixel size of SLM is very small so that $\Lambda \mathrm{sinc}\left(\frac{\Lambda k_x}{2}\right) \Lambda \mathrm{sinc}\left(\frac{\Lambda k_y}{2}\right) \approx 1$. To simplify the formula, we define a normalized momentum-space light intensity

$$I(k_x, k_y) = -\frac{1}{2} \sum_{j,h} \mathrm{e}^{\mathrm{i}\Big((\theta_j - \theta_h) - \big(k_x(x_j - x_h) + k_y(y_j - y_h)\big)\Big)}. \quad \text{(S8)}$$

Furthermore, we multiply the momentum-space light intensity by a modulation function $V(k_x, k_y)$ and integral it over the entire momentum space. By this means, we obtain a new physical quantity:

$$\begin{aligned}
H_k &= \iint_{-\infty}^{\infty} I(k_x, k_y) V(k_x, k_y) \mathrm{d}k_x \mathrm{d}k_y \\
&= -\frac{1}{2} \iint_{-\infty}^{\infty} \sum_{j,h} \mathrm{e}^{\mathrm{i}\Big((\theta_j - \theta_h) - \big(k_x(x_j - x_h) + k_y(y_j - y_h)\big)\Big)} V(k_x, k_y) dk_x dk_y \\
&= -\frac{1}{2} \sum_{j,h} \iint_{-\infty}^{\infty} \mathrm{e}^{\mathrm{i}\Big((\theta_j - \theta_h) - \big(k_x(x_j - x_h) + k_y(y_j - y_h)\big)\Big)} V(k_x, k_y) dk_x dk_y \\
&= -\frac{1}{2} \sum_{j,h} \mathrm{e}^{\mathrm{i}(\theta_j - \theta_h)} \iint_{-\infty}^{\infty} \mathrm{e}^{-\mathrm{i}\big(k_x(x_j - x_h) + k_y(y_j - y_h)\big)} V(k_x, k_y) dk_x dk_y \\
&= -\sum_{j,h} \cos(\theta_j - \theta_h) \iint_{-\infty}^{\infty} \mathrm{e}^{-\mathrm{i}\big(k_x(x_j - x_h) + k_y(y_j - y_h)\big)} V(k_x, k_y) dk_x dk_y.
\end{aligned} \quad \text{(S9)}$$

Clearly, $\iint_{-\infty}^{\infty} \mathrm{e}^{-\mathrm{i}\big(k_x(x_j - x_h) + k_y(y_j - y_h)\big)} V(k_x, k_y) dk_x dk_y = J(\boldsymbol{r}_{jh})$. Comparing Eq. S9 and Eq. S4, we find

$$H_k = -\sum_{j,h} \cos(\theta_j - \theta_h) J(\boldsymbol{r}_{jh}) = H_r. \quad \text{(S10)}$$

Therefore, H_k is the spin Hamiltonian of the XY model represented in the momentum-space of light. This equation can be regarded as a generalized form of the Plancherel theorem, also known as Parseval–Plancherel theory. Let $V(k_x, k_y) = 1$, it can be specified as the conventional Plancherel theorem that describes light diffraction. Otherwise, it connects distinct two-body spin Hamiltonians from momentum-space modulation of light diffraction.

Supplementary Note 2. Experimental Setup

In our experiment, a laser beam at the wavelength of $\lambda = 532nm$ and with a beam width of $1mm$ is expanded 50 times using a telescope system composed of two lenses, L1 and L2, to achieve a uniform amplitude wavefront (see Figure S1). The polarizer and half-wave plate are used to control the incident polarization to align with the modulation polarization of the phase-only SLM. After passing through an optical aperture, the laser beam is split by a beam splitter (BS) into two branches. One branch is modulated by the SLM. The modulated light passes through a lens L3 ($f = 150.5mm$) and is captured by a CMOS camera located in the momentum space. The other branch serves as the reference light. The intensity is also captured by the CMOS camera but at a different area (see Figure S4). This reference light is used to monitor the intensity fluctuation of the optical system to reduce the experimental error. The SLM contains 1920×1080 pixels, with a pixel size of $4.5\mu m \times 4.5\mu m$. In the experiments, we use $M \times M$ pixels as a superpixel to encode a single spin. Specifically, for the J_1-J_2-J_3 model experiments, we used $M = 40$, while for the XY model experiments, we used $M = 20$. The CMOS camera (QHYCCD QHY294M Pro) contains 4164×2796 pixels, with a pixel size of $4.63\mu m \times 4.63\mu m$. The intensity depth for the CMOS pixel is 16 bits. A computer system is used to control the phases of SLM and record the data from CMOS, facilitating real-time feedback during optical computations.

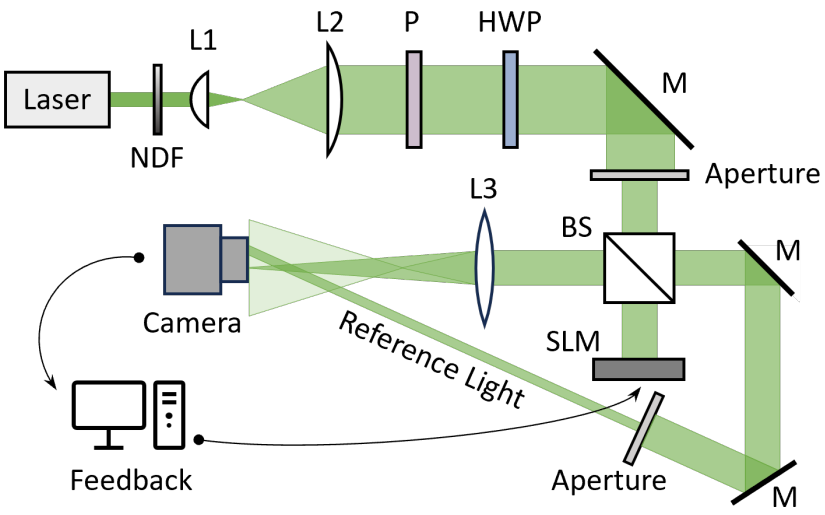

NDF: neutral density filter, L1-3: lens, P: polarizer, HWP: half-wave plate, M: mirror, BS: beam splitter, SLM: spatial light modulator

Figure S1: **Experiment Setup.**

Supplementary Note 3. Noise Analysis in the Experiments

3.1 Choosing the Momentum Space Integral Range

$J(\boldsymbol{r}_{ij})$ represents the interaction between each spin and the other spins. For the case of nearest-neighbor interactions , each spin in the system (represented by the large black dots at the center in Figure S2) interacts with the four neighboring spins located above, below, left, and right. According to Eq.(S4), the ideal integral range of the momentum-space is infinite. In the experiment, we set the integral range of modulated momentum-space as $[-2\pi/\Lambda, 2\pi/\Lambda]$ as a good approximation. Considering the nearest-neighbor (NN) interaction as an example (see Figure S2), the inverse Fourier transform $J'(\boldsymbol{r}_{ij})$ agrees well with the original $J(\boldsymbol{r}_{ij})$. As a comparison, if we set the integral range as $[-\pi/\Lambda, \pi/\Lambda]$, incorrect interactions emerge in $J'(\boldsymbol{r}_{ij})$.

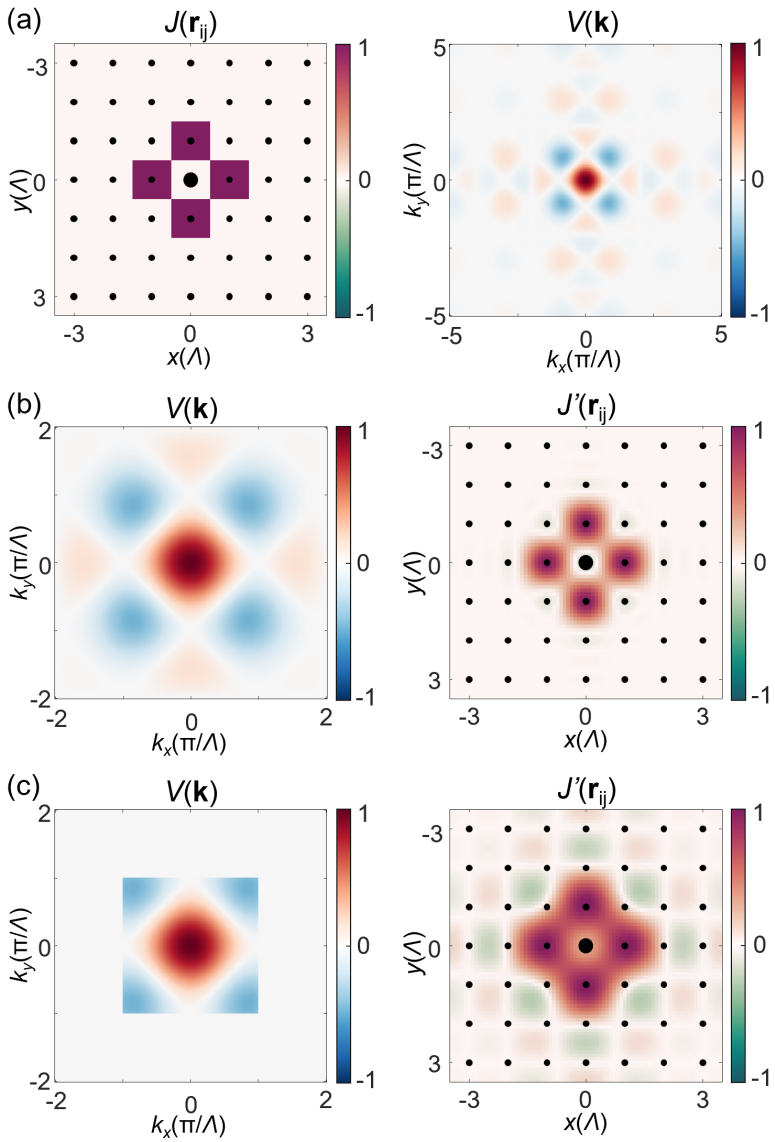

Figure S2: **The impact of the integral range of momentum space on the spin interaction function.** (a) The NN interaction strength function $J(\boldsymbol{r}_{ij})$ and its Fourier transform $V(\boldsymbol{k})$ in the range of $[-5\pi/\Lambda, 5\pi/\Lambda]$. (b) The Fourier transform $V(\boldsymbol{k})$ in the range of $[-2\pi/\Lambda, 2\pi/\Lambda]$ and its inverse Fourier transform $J'(\boldsymbol{r}_{ij})$. (c) The Fourier transform $V(\boldsymbol{k})$ in the range of $[-\pi/\Lambda, \pi/\Lambda]$ and its inverse Fourier transform $J'(\boldsymbol{r}_{ij})$.

3.2 The Influence from the 0-order Diffraction

The SLM has a modulation efficiency of 75%, which means that part of the light will reflect from the SLM without being manipulated. This 0-order diffraction (also known as background) is focused as a point in the center of the momentum space (see Figure S3(b)), severely affecting the calculation precision of spin Hamiltonian. To reduce the noise from 0-order diffraction, we add a Fresnel lens phase front onto the SLM to separate the focal planes of the 0-order diffraction and the modulated light to different locations along the light path. Therefore, at the momentum plane of modulated light, the 0-order diffraction is divergent as a broad and weak background (see Figure S3(c)). By this means, the noise from the imperfect SLM modulation efficiency is significantly reduced.

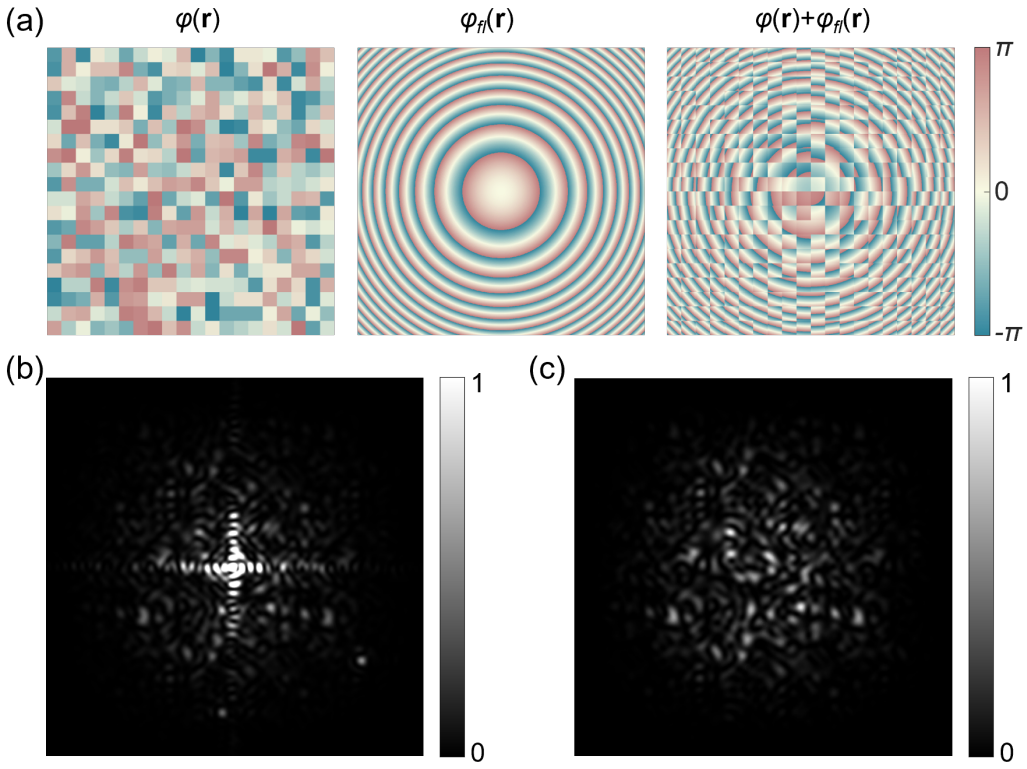

Figure S3: **Superimposing a Fresnel lens phase to reduce the influence from the unmodulated .** (a) left: A random phase distribution $\varphi(\boldsymbol{r})$ encoding the XY spins; middle: A Fresnel lens phase distribution $\varphi_{fl}(\boldsymbol{r})$; right: The phase after superposition $\varphi(\boldsymbol{r}) + \varphi_{fl}(\boldsymbol{r})$. (b) The momentum-space intensity distribution of the random phase-modulated light. (c) The momentum-space intensity distribution of the random phase-modulated light with the lens phase superimposed (background reduced).

3.3 Reducing the Noise From Light Intensity Fluctuations

According to Eq.(S9), the value of H_k depends on light intensity. In the experiment, light intensity fluctuations are inevitable and will introduce calculation errors for H_k. Particularly, this noise is more pronounced for the XY model than the Ising model, as the random flips from the Monte Carlo method will actively induce a much smaller intensity change for the XY model, which can be easily overlapped by the system's random fluctuations. To reduce this noise, we introduced the reference light as depicted in Figure S1. As we split the laser into two branches, one of which serves as the experimental light for Hamiltonian H_k calculations (marked as the red box in Figure S4). The other branch acts as reference light, illuminating a separated range on the CMOS camera (marked as the blue box in Figure S4). If we focus the reference light directly onto the camera, it is more likely to cause overexposure and introduce noise due to the beam's spatial vibrations. Therefore, we directed the plane wave (larger reference beam) onto the CMOS camera. Additionally, by increasing the light intensity, we can reduce the background noise. The CMOS camera simultaneously captures the momentum-space intensity $I(\boldsymbol{k})$ and the reference light intensity I_{ref}. The experimentally calibrated Hamiltonian H_k is calculated using

$$H_k = \frac{\iint_{-\infty}^{\infty} I(k_x, k_y) V(k_x, k_y) dk_x dk_y}{\iint_{-\infty}^{\infty} I_{ref} dk_x dk_y}. \tag{S11}$$

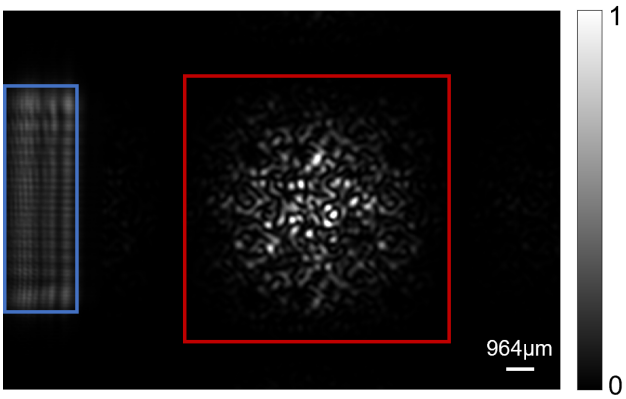

Figure S4: **The momentum-space intensity distribution and the reference light.** The momentum space is the red box region and the reference light illuminates the blue box region.

As an example, we have shown the measured light intensity and the calculated H_r in Figure S5 (a) and (b) for 1000 iterations. It can be seen that the intensity fluctuates by approximately 6%. Although this fluctuation range is small for linear optics, it is critical in the spin model simulator to determine the dynamics of the spin configuration, which is very sensitive to Hamiltonian fluctuation. The H_r is calculated by extracting the phase distributions from the SLM, hence it is not affected by the intensity fluctuations in the momentum space. Therefore, an indication of the noise level from intensity fluctuations can be revealed by the experimentally observed linear correspondence between H_r and H_k. Figure S5 (c) and (d) display the H_k with and without using reference light, respectively. Notably, the error in H_k is smaller using the reference light, as can be seen by the improved goodness of fitting from the coefficient of determination R^2.

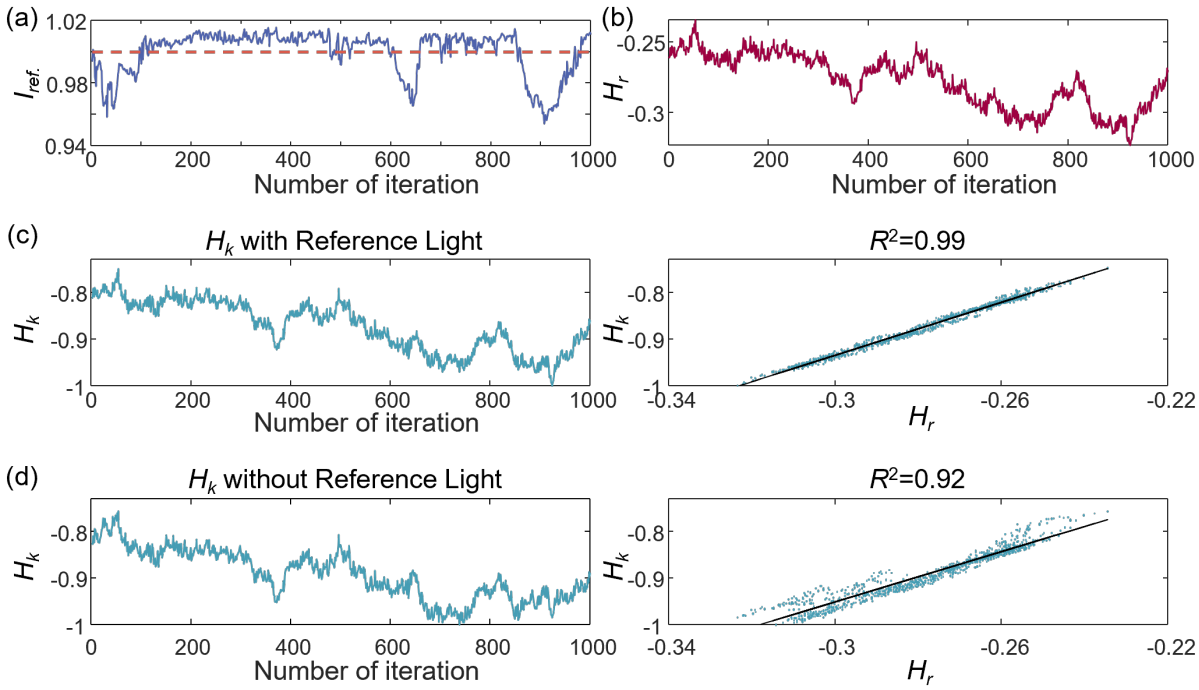

Figure S5: **The impact of light intensity fluctuations on the calculation of H_k.** (a) The monitored light intensity fluctuations. The dashed line is the averaged value over 1000 iterations. (b) The recorded Hamiltonian H_r. (c) left: The observed H_k with a reference light; right: the H_r and H_k correspondence. (d) left: The observed H_k without a reference light; right: the H_r and H_k correspondence. The black lines are linear fitting lines.

3.4 Momentum Space Alignment Method in Experiments

We use a four-point marker method to align the system, ensure that $V(\boldsymbol{k})$ is spatially matched with $I(\boldsymbol{k})$ with small deviation (Fig. S6). The marker points are positioned at $(\pm\pi/\Lambda, \pm\pi/\Lambda)$, which are experimentally generated with holography, as shown in Figure S6(b). In our experiments, the radius of each marker spot is approximately $\delta k = 30\mu$m, while the side length of the measured rectangular momentum space is about $\Delta K = 4280\mu$m. Thus, the maximum misalignment error is about $\delta k/\Delta K \sim 0.7\%$.

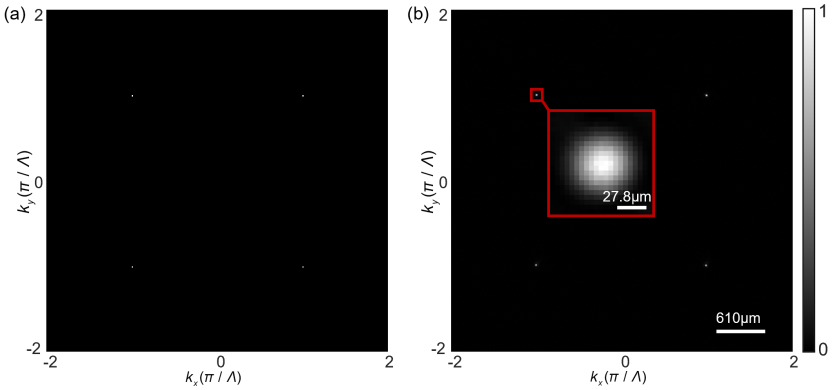

Figure S6: **Four-point marker method to align momentum space**

3.5 Analysis of the Impact of Lens Aberrations in Experiments

Our system operates under the paraxial approximation, where the aberrations are small and negligible. This is further confirmed by the good agreement between theory and experiment. Additionally, we performed calculations to estimate the performance of our imaging system in both aberrated and ideal Fourier transform cases. The results are presented in Figure S7. Using different random phases as input spin configurations, we calculated the aberration case with the spherical wavefront of our lens. In comparison, the non-aberration case was calculated using the ideal Fourier transform. The results show a strong linearity between the two cases, indicating that the impact of aberration is small.

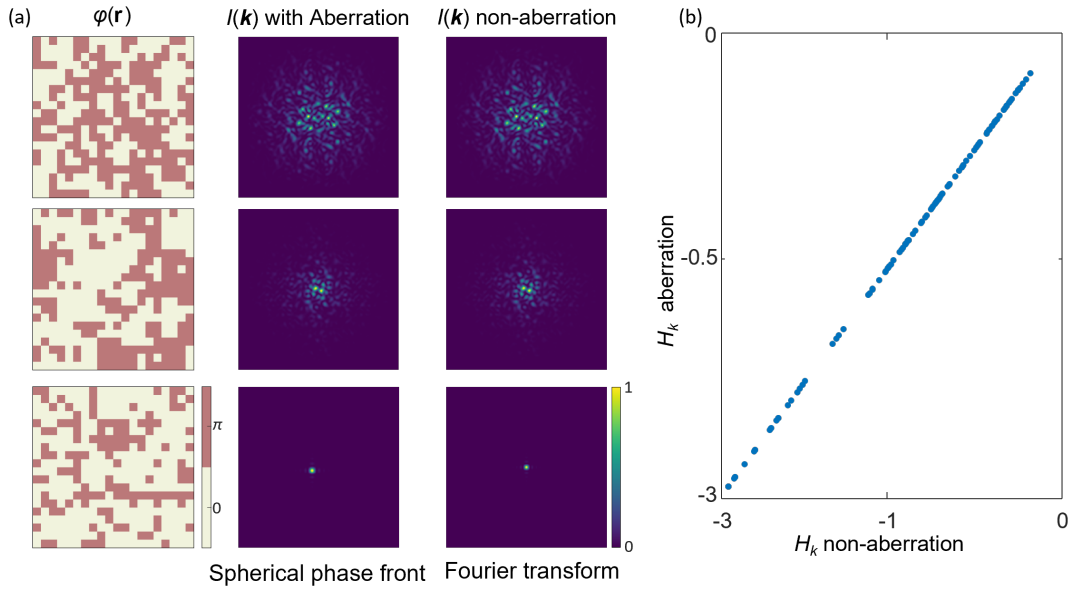

Figure S7: **Analysis of the impact of lens aberrations in experiments.** (a) Calculated $I(\boldsymbol{k})$ from different random phase distributions. The aberration $I(\boldsymbol{k})$ are obtained from spherical phase front of the lens and the non-aberration $I(\boldsymbol{k})$ are obtained from Fourier transform. (b) The resulted linearity between the two calculation methods.

Supplementary Note 4. The Flow Charts of Optical Simulator

Figure S8 and Figure S9 illustrate the quenching and annealing procedures of the spin model simulator, respectively. Prior to the annealing experiment, a quenching experiment is performed to determine an experimental fitting factor f_1 that links H_k and H_r by $H_k = f_1 H_r$, depending on the light intensity, super-pixel size, lens focus distance, camera settings, etc. After the f_1 factor is determined, we can implement optical annealing using the Metropolis algorithm.

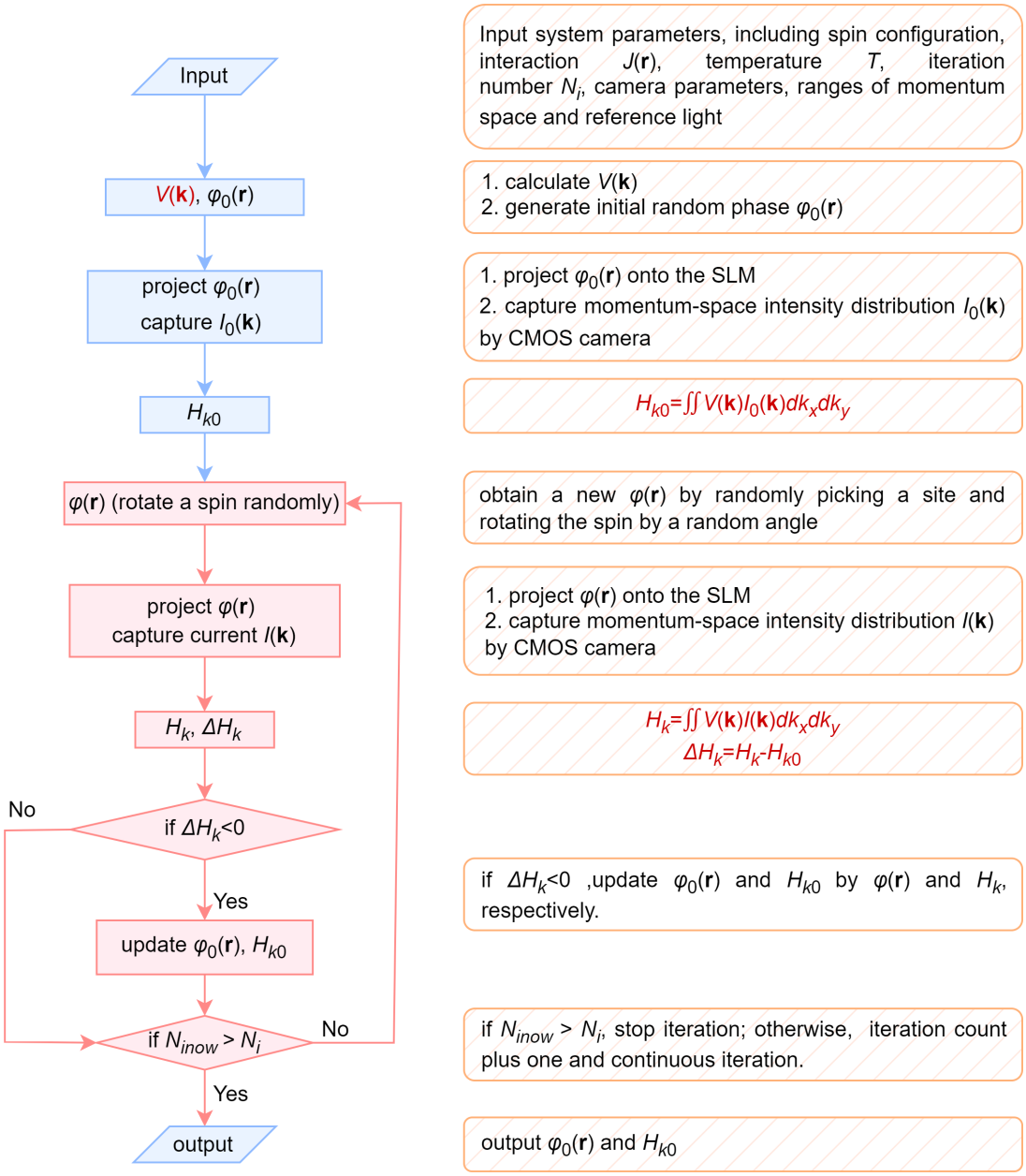

Figure S8: **The flow chart of quenching experiment in the optical simulator.**

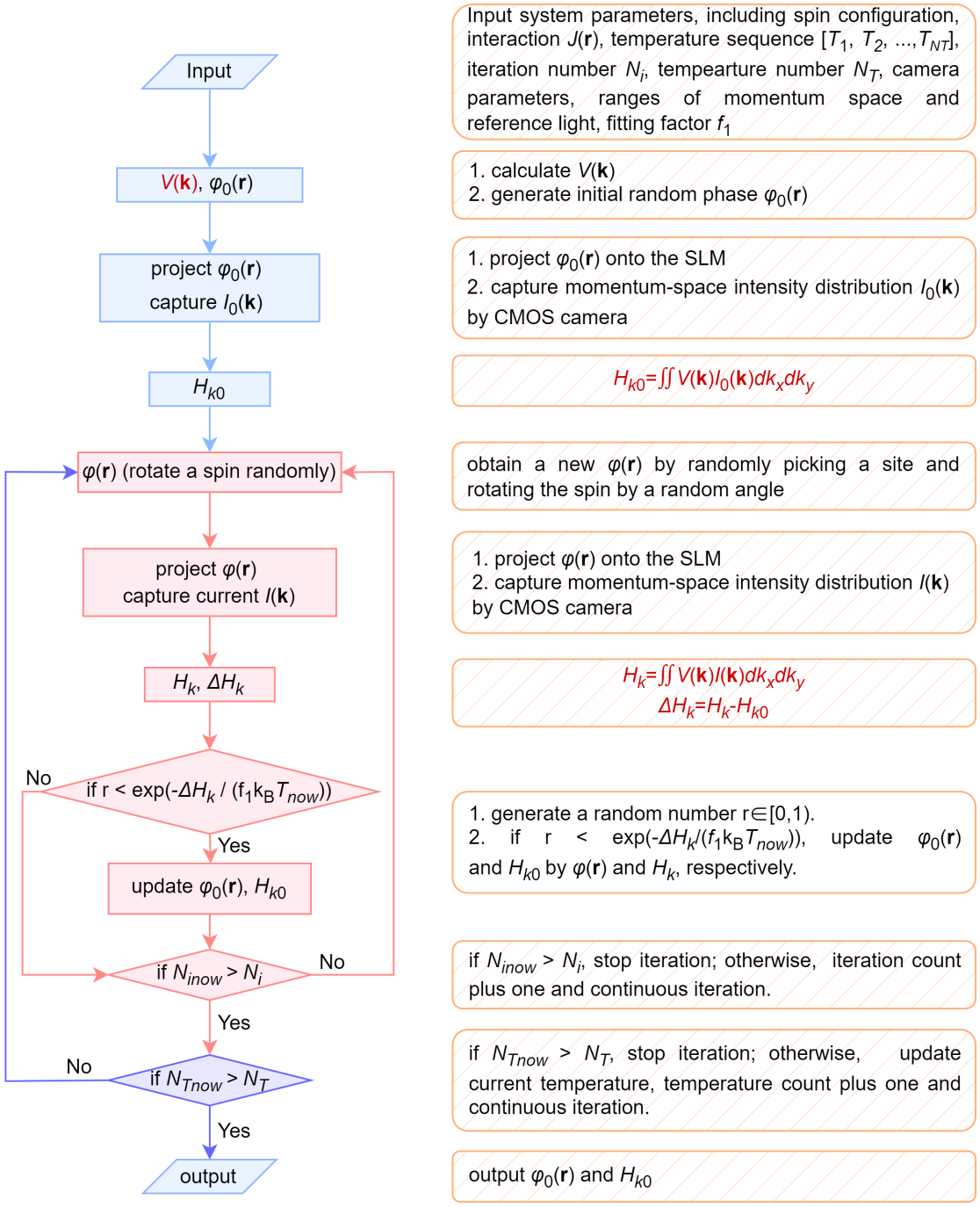

Figure S9: **The flow chart of annealing experiment in the optical simulator.**

Supplementary Note 5. Spin and Momentum-space Light Evolution During the J_1-J_2-J_3 Model Optical Annealing

We selectively show the experimentally observed spin $\varphi(\boldsymbol{r})$ and corresponding momentum-space intensity distributions $I(\boldsymbol{k})$ of the J_1-J_2-J_3 model with different interactions during the annealing process at various temperatures.

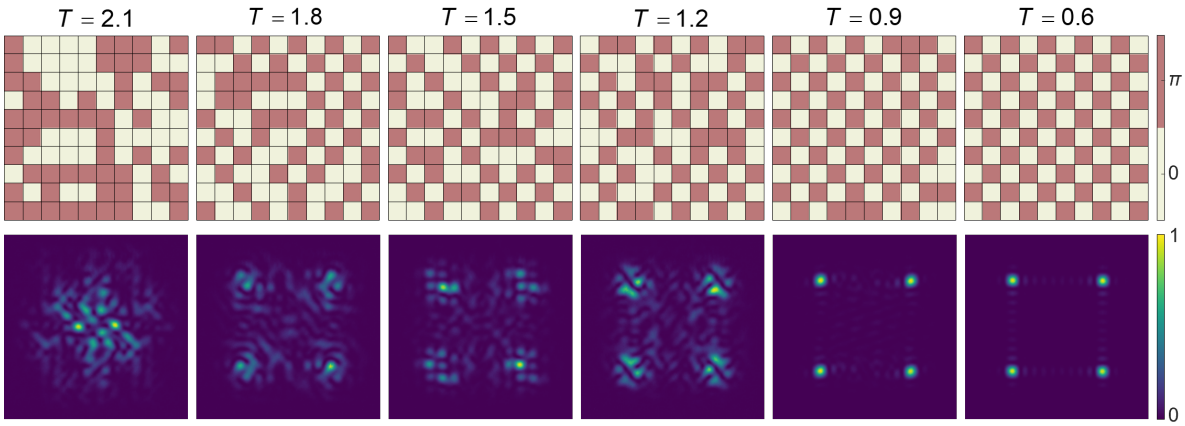

(a) $R_1 = 0.1, R_2 = 0.1$

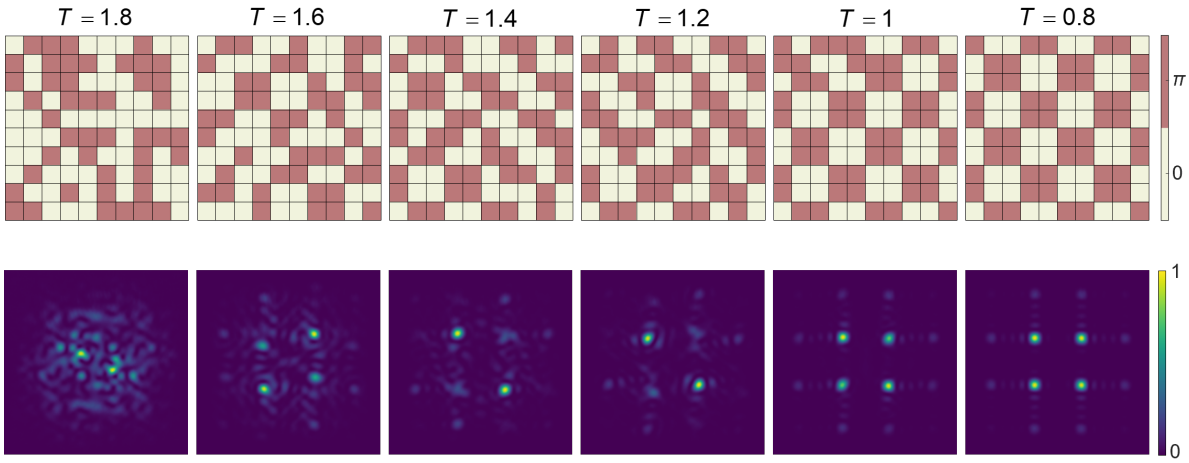

(b) $R_1 = 0.5, R_2 = 0.9$

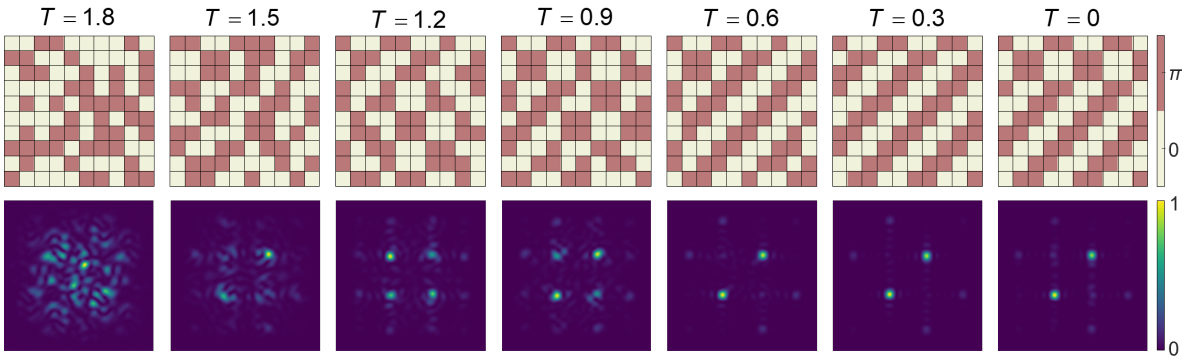

(c) $R_1 = 0.5, R_2 = 0.9$

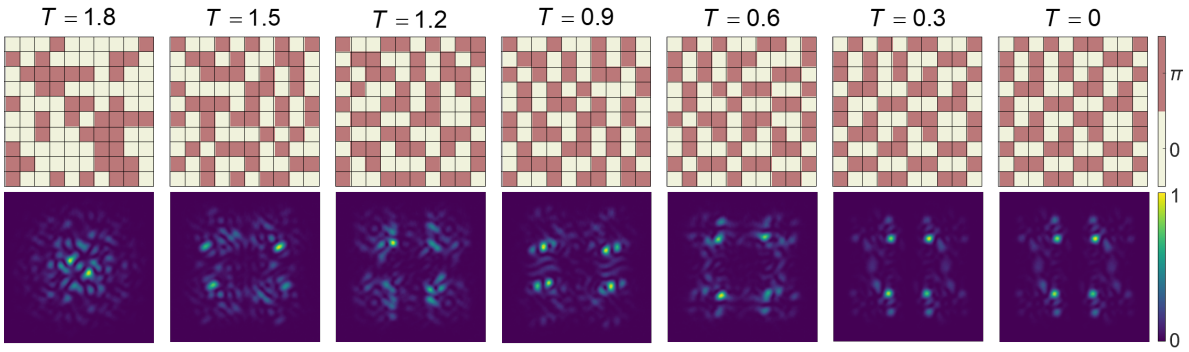

(d) $R_1 = 0.5, R_2 = 0.3$

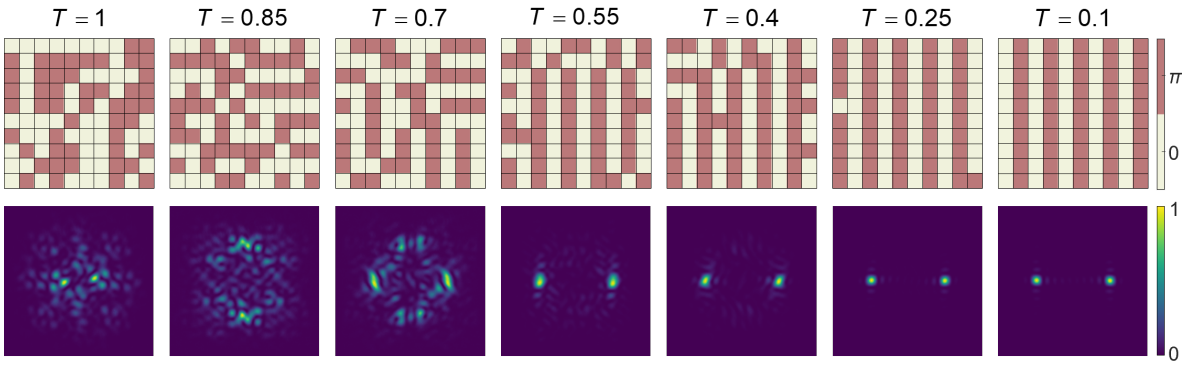

(e) $R_1 = 0.9, R_2 = 0.1$

Figure S10: **The experimental spin $\varphi(\boldsymbol{r})$ and corresponding momentum-space intensity distributions $I(\boldsymbol{k})$ of the J_1-J_2-J_3 model with different interactions during the annealing process at various temperatures.**

Supplementary Note 6. Calculating the Number of Vortices in BKT Dynamics

To visualize the vortex distributions and precisely count the number of vortices, the interpolation divides the interval between two phase values along each dimension by N_{in} times, forming a finer grid, and linear interpolation is then performed on this grid (Figure S11). As the number of interpolations increases, the vortex gradually becomes more distinct and easier to be observed. Figure S12 shows coarsening process during the XY model quenching in main text.

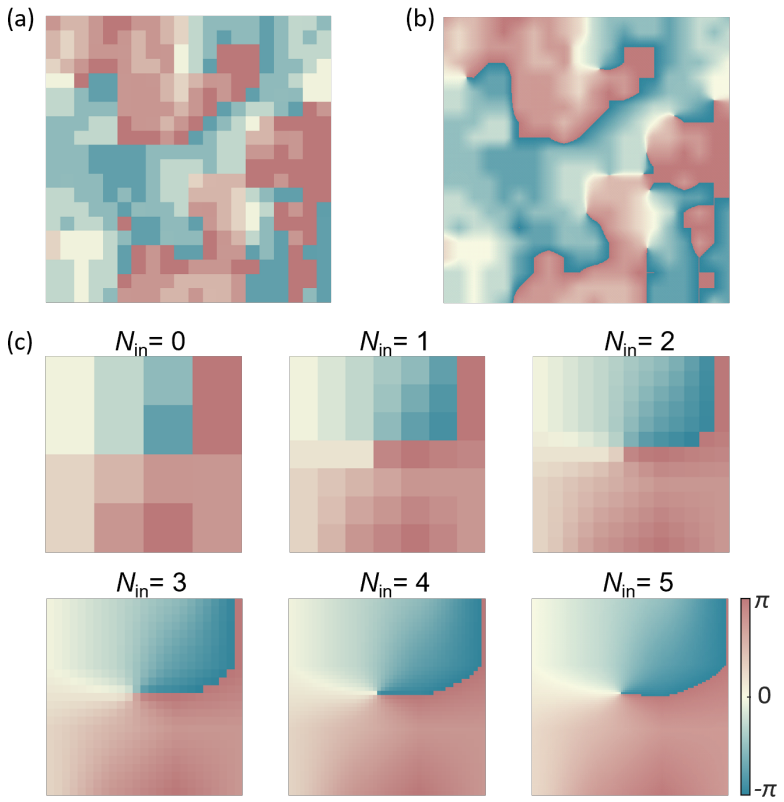

Figure S11: **Phase interpolation method.** The interpolation divides the interval between two phase values along each dimension by N_{in} times, forming a finer grid, and linear interpolation is then performed on this grid. As the number of interpolations increases, the vortex gradually becomes more distinct and easier to be observed.

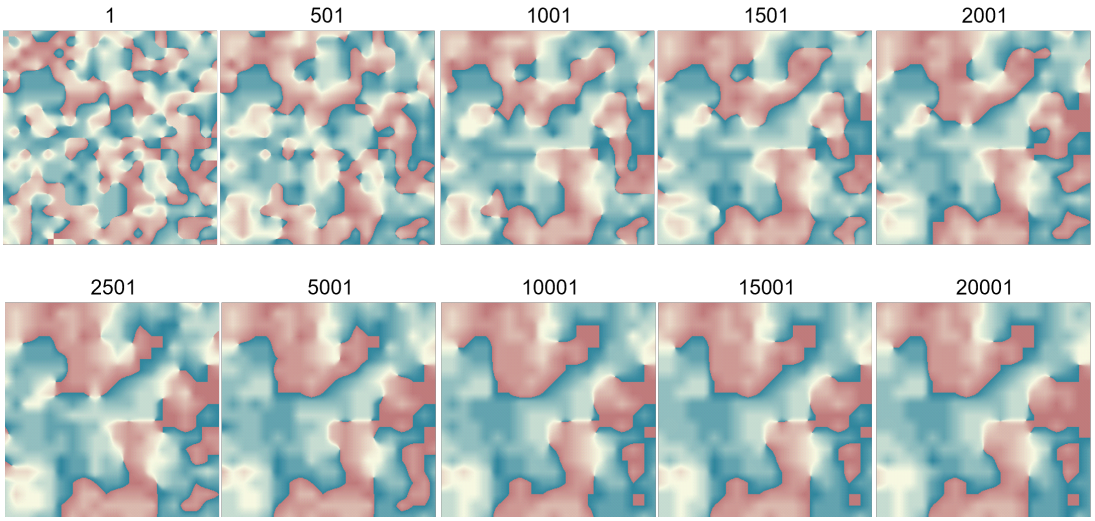

Figure S12: **Coarsening process during the XY model quenching.**The numbers displayed on the top of the pictures are iteration counts.

The method to calculate the vortices is as follows: First, we compute the phase difference between adjacent phases around a given point, $\Delta\varphi_i = \varphi_{i+1 \bmod 8} - \varphi_i$ (Figure S13). If $\sum_1^8 sign(\Delta\varphi_i) = \pm 6$, it indicates that the phase around this point is either increasing or decreasing. Additionally, if the sum of the absolute phase differences $\sum_1^8 |\Delta\varphi_i| = 2\pi$, a

vortex is detected. To avoid double-counting vortices due to numerical errors, we use a breadth-first search (BFS) algorithm, ensuring that each vortex is counted only once. The interpolation number, N_{in}, has a samll effect on the vortex count. For values of $N_{in} > 2$, the vortex count stabilizes (Figure S14).

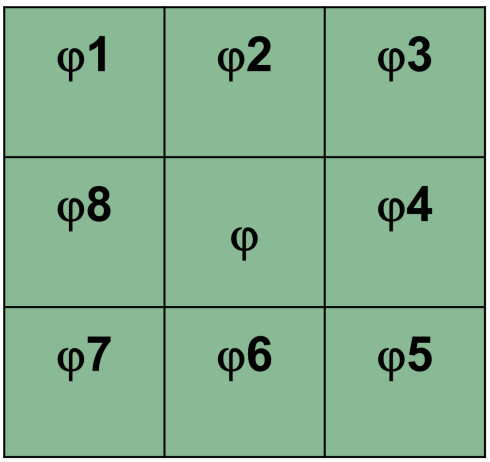

Figure S13: **The method to extract the number of vortices.**

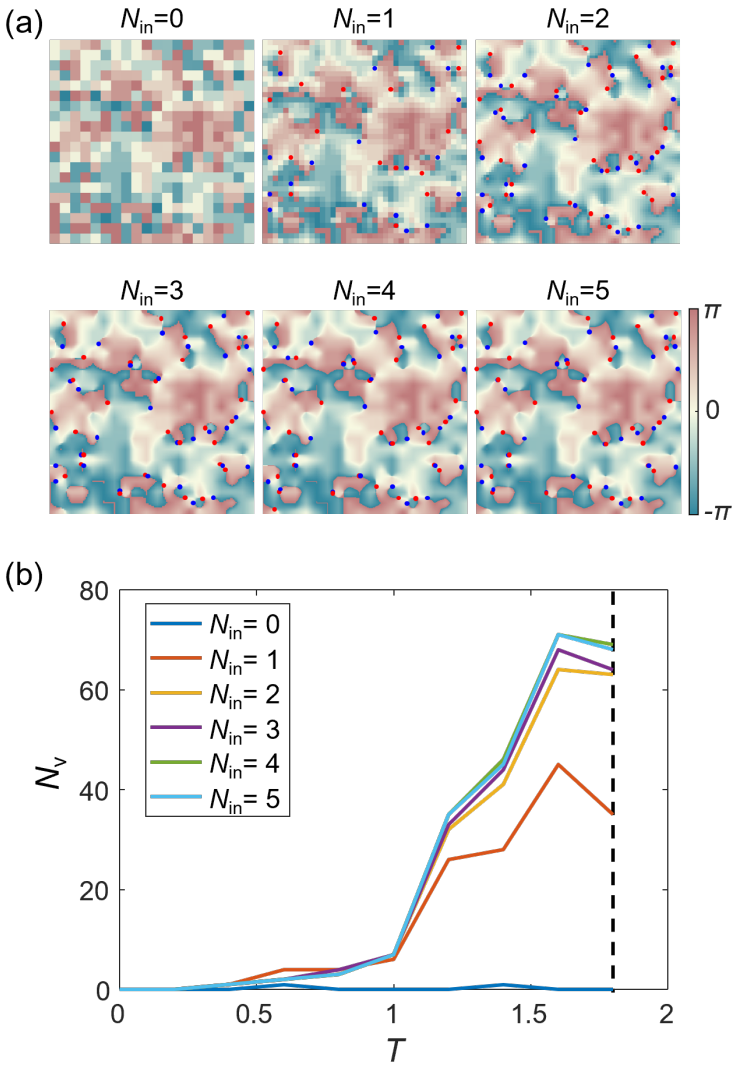

Figure S14: **The impact of interpolation on the calculation of the number of vortices.** (a) Spin distributions interpolated by different interpolation numbers of interpolated points corresponding to the black dashed line in (b). Red and blue dots represent clockwise and anticlockwise vortices, respectively. The numbers on the top of the pictures are interpolation numbers N_{in}. (b) The calculated number of vortices of different numbers of interpolated points.

Supplementary Note 7. Quenching Experiments of Ferromagnetic Ising Models with NN Interaction and 7NN Interaction

We performed additional experiments to show the quenching processes of the ferromagnetic Ising models with a typical NN interaction, and a typical long-range interaction (7NN). These experiments are important evidence to demonstrate our spin model simulator as a useful tool to explore various spin models ranging from short-range to long-range interactions. For short-range interactions and long-range interactions, they correspond to different $V(\boldsymbol{k})$ in momentum space (see Figure S15 (a,b)). Specifically, for an all-to-all in-

teraction where $J(\boldsymbol{r}_{ij})$ is constant in the real space, V(k) becomes a Dirac delta function. In this case, there is no phase transition. For the NN interaction, a phase transition occurs at a Curie temperature T_c about $2.269J$, where J represents the interaction strength. If $T > T_c$, the spin system is in a disordered phase; if $T < T_c$, it transits to an ordered phase. In our experiments, the NN interaction and 7NN interaction systems both evolve to the ordered phase at the quenching temperature $T_1 = 0$ (see Figure S15 (c)). However, due to the short-range nature of NN interaction, it exhibits more magnetic domains. At the quenching temperature of $T_2 = 4$, the 7NN interaction system still evolves to an ordered phase, indicating a lack of phase transition in long-range interaction systems. Meanwhile, the 7NN interaction system evolves to a disordered phase (see Figure S15 (d)). These experimental results agree well with theoretical predictions.

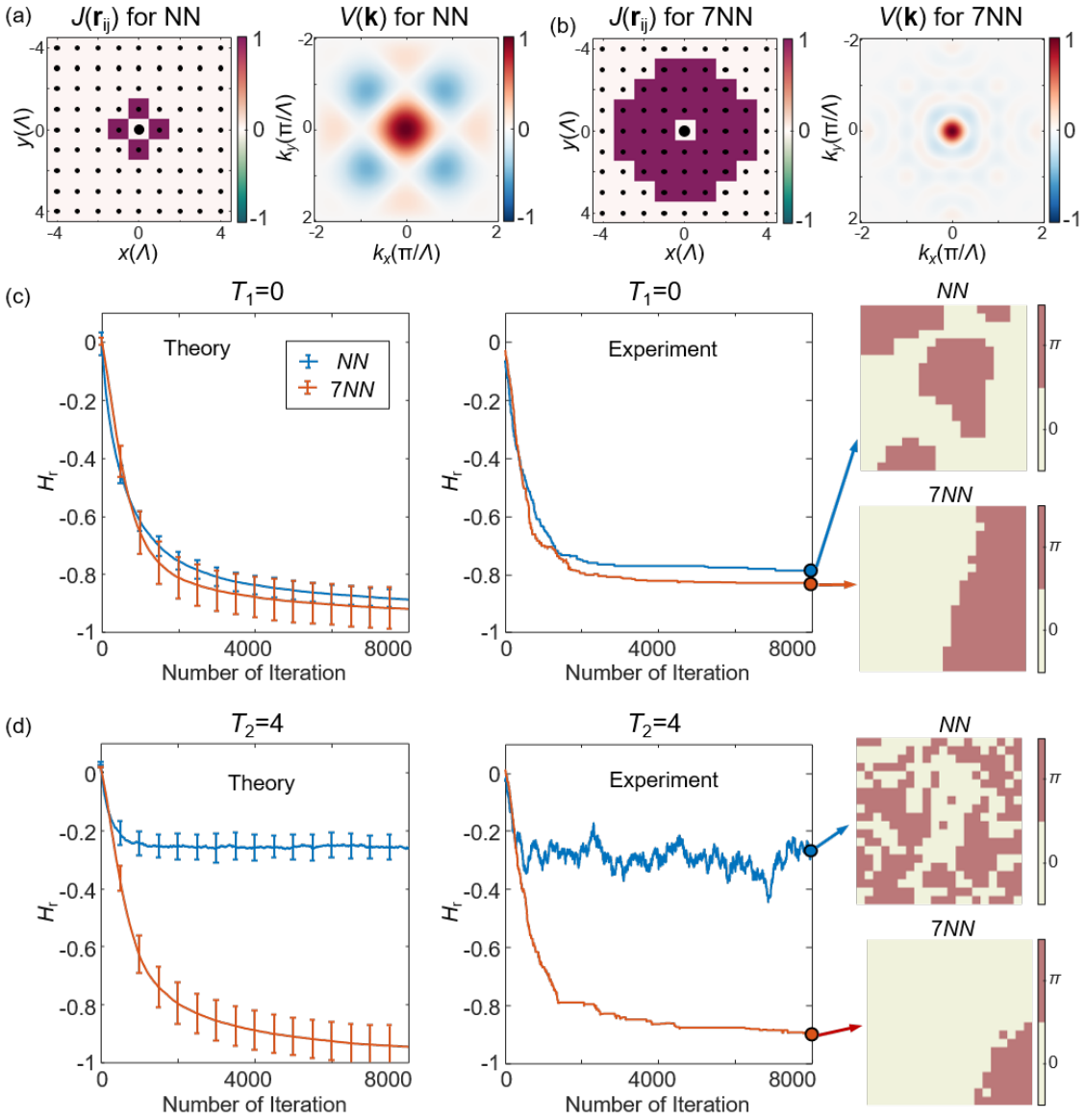

Figure S15: **Quenching experiments of the Ising model with NN interaction and 7NN interaction.** (a)(b) The (a) NN and (b) 7NN interaction strength functions $J(\boldsymbol{r}_{ij})$ and the corresponding Fourier transforms $V(\boldsymbol{k})$. (c)(d) The simulated and experimental quenching process of the Ising model with NN interaction and 7NN interaction at the temperature (c) $T_1 = 0$ and (d)$T_2 = 4$. Simulated results are obtained from statistical calculations. The graphs on the far right side are the final spin distributions from the experiments.

Supplementary Note 8. The method for realizing arbitrary interactions

In the experiments described in the main text, we map the spins onto the SLM using a standard method, employing square lattices (as in the J_1-J_2-J_3 and XY models). We observe that both the spin-spin interaction function $J(\boldsymbol{r}_{ij})$ and the function $V(\boldsymbol{k})$ exhibit centrosymmetry. To achieve non-centrosymmetric or uniquely defined interactions between spin pairs, we can map the spins onto different lattice structures on the SLM.

These types of modulations can be experimentally implemented using an amplitude-and-phase SLM or by utilizing an additional phase-front encoding approach, as described in Figure S3.

In Figure S16 (a), non-centrosymmetric interactions are achieved by adjusting the distances between adjacent spins. In the second case shown in Figure S16, the displacements $\boldsymbol{r}_{ij}$ are assigned randomly for different spin pairs, making $\boldsymbol{r}_{ij}$ unique for each pair. As a result, we can assign $J(\boldsymbol{r}_{ij}) = J_{ij}$ as unique values for each pair. However, it is important to note that the maximum number of spins that can be encoded on the SLM is reduced. In the most general case, the maximum number of spins decreases from L^2 (the number of pixels on the SLM) to L.

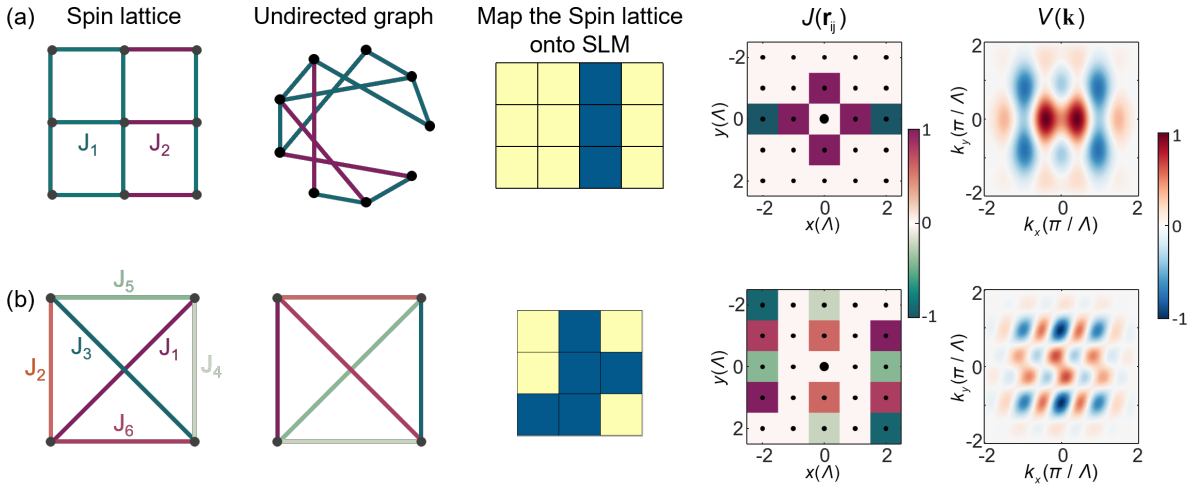

Figure S16: **Spin systems with asymmetric and arbitrary spin interactions.** (a) An example of an non-centrosymmetric spin interaction. (b) An example of arbitrary spin interaction. For the connected 4 spins, there are C_4^2 =6 unique spin interactions, corresponding to the 12 colored pixels in the $J(\boldsymbol{r}_{ij})$map. The $J(\boldsymbol{r}_{ij})$ colormap is shown for $\boldsymbol{r}_i = 0$ (the central black spot).

Supplementary Note 9. Experimental validation of system scalability

We conducted two sets of experiments to demonstrate the scalability of our system by varying the number of spins, L^2, and the super-pixel size, M. The results are shown in Figures S17 and S18. Both sets of experiments were based on the nearest-neighbor interaction Ising model, where we compared the optically computed Hamiltonians (H_k) with the numerical calculations (H_r) to evaluate the accuracy of our system. The optically measured H_k and the calculated H_r values are represented by dots, with fitted lines for comparison. Selected $I(\boldsymbol{k})$ are shown in the lower panels.

To quantify the prediction accuracy of H_k relative to H_r, we used the coefficient of determination, R^2. Notably, an R^2 value approaching 1 indicates a good linear fit, with $R^2 = 1$ representing a perfect prediction. For these experiments, the R^2 values were very

close to 1, demonstrating excellent accuracy across various spin sizes. These results suggest that the measurement precision remains consistently high, regardless of changes in system scale or super-pixel size.

In summary, the experimental results validate the strong scalability and robustness of our system, maintaining precise measurement accuracy under varying experimental conditions.

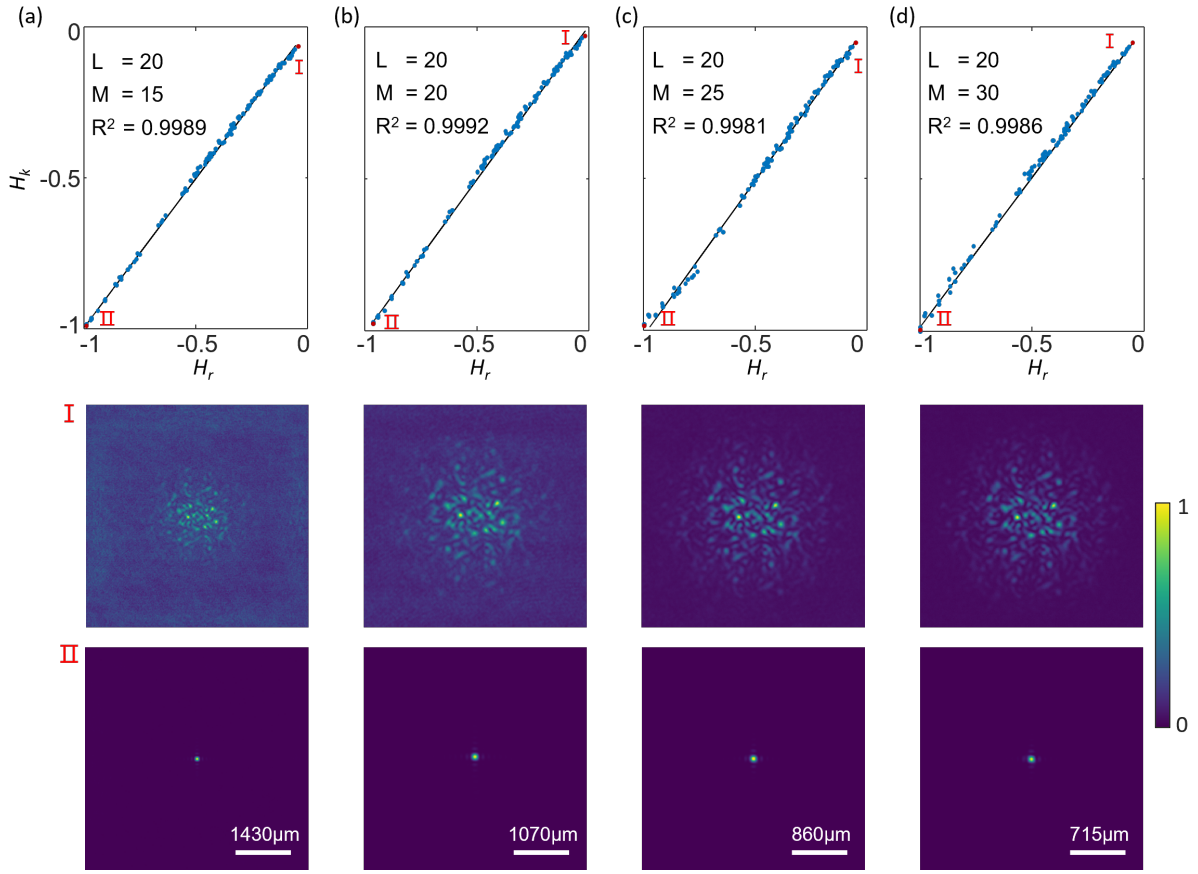

Figure S17: **Experimental Performance with different number of super-pixel M and spin numbers $L^2 = 400$.** (a) $M = 15$; (b) $M = 20$; (c) $M = 25$; (d) $M = 30$. The lower panels are selected experimental $I(\boldsymbol{k})$.

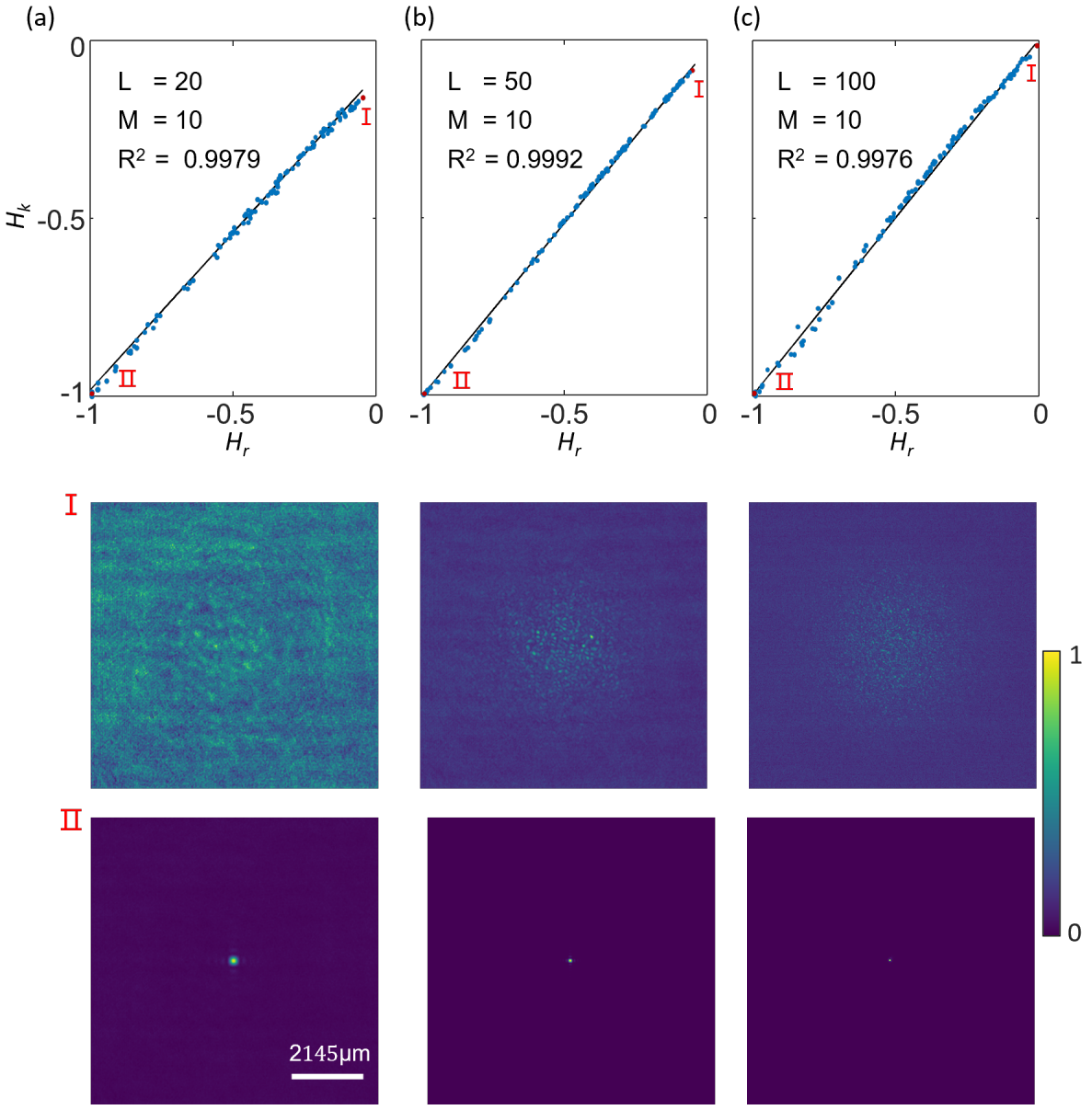

Figure S18: **Experimental Performance with different spin numbers L^2 and number of super-pixel** $M = 10$.(a) $L^2 = 400$; (b) $L^2 = 2500$; (c) $L^2 = 10000$. The lower panels are selected experimental $I(\boldsymbol{k})$.